

## Friction Stir Welding with low-medium-high Tool travel speed of 0.95 Mg-Al-alloy and pure Copper: Electrochemical and Surface studies

Neetesh Soni<sup>1,2</sup>, Ambrish Singh<sup>1,2\*</sup>

<sup>1</sup>School of Materials Science and Engineering, Southwest Petroleum University, 8 Xindu district-610500, Chendgu city, Sichuan province, China.

<sup>2</sup>State Key Laboratory of Oil and Gas Reservoir Geology and Exploitation, Southwest Petroleum University, Chengdu, Sichuan 610500, China.

**\*Corresponding author**

**\*E-mail:** [vishisingh4uall@gmail.com](mailto:vishisingh4uall@gmail.com); [drambrishsingh@gmail.com](mailto:drambrishsingh@gmail.com)

**Ph.no.** +86-18384155035

### ABSTRACT

The aim of this work is to assess the influence of Friction Stir Welding (FSW), process parameters, optimized tool traveling speed, and corrosion resistance of the 0.95 Mg-Al-alloy and pure copper weldment. Samples of aluminum-copper with and without deformation were characterized to investigate the metallurgical effects created during the welding deformation process. Effect of process parameters on microstructure and corrosion rate have been investigated for all the samples. All the electrochemical and polarization tests were done in 3.5 wt.% NaCl solution. Scanning Kelvin Probe (SKP) was done to detect the localized corrosion on the surface. Optical micrography observation indicated that the primary  $\alpha$ -Al phase, which was formed during solidification can effectively limit the growth of  $\text{Cu}_9\text{Al}_4$  phase. Finer acicular  $\alpha$ -Al precipitates were observed in CuAl matrix during joining process that tends to coarser with the increase in tools travel speed. The electrochemical and polarization results showed that among all the tool travelling speed the specimen joined at tool travelling speed of 40 mm/min shows the best non-corrosive property.

**Key words:** Friction Stir-Welding; Aluminum-Copper; SKP; Corrosion test; Electrochemical; Tool travel speed

## 1. INTRODUCTION

Nowadays, the emerging trend is to join dissimilar metals by friction stir welding [1]. The dissimilar joints such as Aluminum-Copper, Al-Steel, Al-Magnesium in recent decades is eye catching, because of its huge demand in various industries. Industries are more focused on these types of joints due to enhanced durability, reduction in the weight percentage of materials, and cost effectiveness. In the last two decades 0.95 Mg-Al-alloy and copper dissimilar joint have become the backbone of industries. These joints are mostly used in aircraft electric coupling, electric coupler in oil and gas industries, high speed trains, heat exchanger, electrical heavy load (power) supply and connectors of hydraulic pistons. As per the report of IACS (International annealed copper standard) copper shows a better percentage of conductivity (100%) after silver (105%). Copper is very expensive as compared to aluminum and aluminum alloy also has good percentage of conductivity (61%) after gold (71%) [2]. So, this was our motivation to use 0.95 Mg-Al-alloy with 61% percentage of conductivity. 0.95 Mg-Al-alloy and pure copper bimetallic joint is economic and saves enormous costs for industries. It has better strength, higher workability, and good corrosion resistance [3]. The dissimilar joint fabricated by friction stir welding of aluminum-copper avoids the inhomogeneity of microstructural properties, obtains higher mechanical properties and fulfills performance parameters of electrochemical properties compared with other welding techniques [4]. During the Friction stir welding, formation of intermetallic precipitate and its distribution along the weldment matrix enhances the galvanic corrosion. The reduction in the grain size in the weldment region influences the rate of corrosion [5].

The majority of previous study shows [6] the effect of generated temperature and microstructural assessment of the friction stir welding of 0.95 Mg-Al-alloy to copper. Some intermetallic compounds formed were identified during welding such as  $\text{CuAl}_2$ ,  $\text{CuAl}$ ,  $\text{Cu}_9\text{Al}_4$  with little quantities of  $\alpha$ -Al and the saturated solid solution (SSS) of aluminium in copper. The peak temperature observed in the weld zone was around  $580^\circ\text{C}$ . Investigation of the low, medium, and high rotational speed with the respective feed rate illustrated that the medium tool rotational rate and 30mm/min tool traverse speed gives better microstructural and mechanical properties compared to other parameters [7]. Enhancing the travelling speed of tools decreases the grain structures of weld zone; this can be depicted by comparing the XRD patterns of the base metals and welded samples [8]. Fabrication of friction stir welding of aluminum-copper generates internal

residual stress (IRS) in the dynamic recrystallized zone (DXZ) causing modifications in the electrochemical and mechanical properties of weldment [9-11]. This is influenced by the process parameters of machine setup and is also affected by the composition of base materials [10] identified in the region where corrosion occurs. 2024-T3-Al alloys joined by friction stir welding were examined through corrosion study concluding that highest corrosion rate was observed in DXZ than Base material (BM) and Thermomechanical Affected-Zone (TMA-Zone) because of the formation of intermetallic compounds due to the elements present in the alloys [11]. Preceding research have shown that the welding parameters such as travel speed of tools, rotational speed of tools is affected by the rate of corrosion during the examination of 2024-T351-Al alloys in the 0.1 M NaCl solution [12]. Moreover, in the dynamic recrystallized zone the attack by the intergranular corrosion is high at very low rotation of tool speed (215 rpm) compared to thermomechanical affected-zone and base metal. Corrosion due to higher rotational speed of tool during friction stir-welding was investigated and a conclusion was drawn that the feasibility for the enhanced corrosion resistance was absence due to lack of  $Al_2Cu$  phase in the dynamic recrystallized-zone [13]. Corrosion resistance is better in the alkaline solution for the weldment region of dynamic recrystallized -zone (DXZ) and selection of higher tool rotational speed during friction stir-welding enhances the fabrication of 2219-O-Al Alloys joint [14]. The tool pin profile also affects the corrosion resistance properties and the generation of heat influences the corrosion resistance of 2219-Al alloy [15]. The elevated temperature due to heat generation is useful in avoiding the  $Al_2Cu$  particles and enhancing the corrosion resistance.

Both aluminum and copper are incompatible metals although they show a high affinity to each other at temperatures higher than  $120^{\circ}C$  and produce brittle intermetallic on the interface when joined together. Very few researchers focused on joining of aluminum-copper for electrochemical investigation. The available data for the research work done on FSW of dissimilar metals did not represent systematic study to characterize the microstructural formation. The properties of dissimilar welds, effects of temperature, material flow and interaction is also not well reported or discussed. In current work, a feasibility study of joining 0.95 Mg-Al-alloys to pure copper plates of 3 mm thickness by friction stir welding was performed. The systematic study was conducted to analyze the welded 0.95 Mg-Al-alloy with pure Cu joints by friction stir welding- XRD study, micro hardness and SEM to study the corrosion of the weldments.

## **2. Experiment**

### **2.1. Selection of materials with elemental analysis**

The sheet dimensions of 3 mm thickness were used of 0.95 Mg-Al-alloys and pure copper to perform the materials elemental analyses. The study was carried out using test method for copper with MDD/SOP/Cu and OES/DV-6 equipment and for 0.95 Mg-Al-alloy test method following the ASTM/E1251 standard. All the materials elemental analyses were done in DRDL/CHEM/MDD Hyderabad as represented in Table 1. Due to the limitation of the test material, 0.95 Mg-Al-alloys plates of 260×60×3 dimension as well as pure copper plates of 260×60×3 dimension were taken in the form of rolled plate.

### **2.2. Selection of tool materials with chemical composition**

In this investigation, AISI- H13 tool steel is chosen as tool material. The AISI-H13 tool steel owns good strength and firmness at elevated temperature, wear resistance, suitable toughness, thermal fatigue strength, heat cracking resistance, machinability, availability, is cheap and the typical chemical composition of AISI-H13 tool steel is presented in Table 2.

AISI-H13 tools were made with the 24 mm shoulder and 20 mm collet diameter with tapered threaded pin profile (Ø6 mm, 2.7 mm in length). Selected rotation of the tools was 1350 rpm angled at 2°, with fixed traveling speed of 30, 40, and 50 mm/min, respectively.

### **2.3. Sample preparation and Mounting**

An area of 1.5 cm × 1.5 cm was cut from the welded sample containing the Al-HAZ-TMAZ-DXZ-TMAZ-HAZ-Cu zones. The samples were mechanically abraded using 120 to 600 grit SiC papers and were polished using diamond paste. After polishing etching was performed using two different etchants for copper (distilled water-100 ml, HCl-15 ml, and ferric chloride-2.5g) and for 0.95 Mg-Al-alloy (HF-2 ml, HCl-3 ml, HNO<sub>3</sub>-5 ml distilled water-190 ml). The samples were then exposed to the electrochemical studies and the corrosion tests were conducted. The corroded area was studied using XRD-Cu-K<sub>α</sub> radiation, optical microscopy and SEM.

### **2.4 Micrography Examination**

Microstructures of the samples were studied using Leitz optical microscope. Huvitz upright Microscopes HRM-300 series was used to study the weldment structure of the cross-section region.

The specimens of 30×3 mm size were cut from the middle of all the samples for microhardness analysis.

### **2.5 Microhardness analysis**

The test was performed using Vickers digital microhardness tester (Model: Autograph, Make: Shimadzu) with a 200 g load for the duration of 15 seconds. The pattern for micro hardness using Vickers digital machine is shown in Figure 1. The microhardness was tested at the interval of 0.15 mm across the unaffected base metal, processed zone, thermo-mechanical affected zone, and the heat affected zone.

### **2.6 XRD examination of welded samples**

The phase analysis of the dissimilar welded sample of 0.95 Mg-Al-alloy and pure copper welded samples were carried out by the X-ray diffraction technique. The diffraction spectrum obtained from the XRD technique has been analyzed using the PANalytical X'pert Highscore plus software (it is a database containing the peak XRD data for all the elements in the periodic table and their compounds). The peak shift for the 0.95 Mg-Al-alloy and pure Cu metal at scan range of 10° to 120° angle with scan step is 0.01 for the identified accurate peak on welded surfaces.

### **2.7 Electrochemical analyses**

The electrochemical examinations for the all specimens were accomplished at room temperature in 3.5 wt.% NaCl solution. The bare surface area to the aggressive solution was 1cm<sup>2</sup>. The impedance and polarization experiments were carried out using Autolab workstation.

The tests were carried out in an assembly of three electrode cell according to the ASTM: G69 standard with an Ag/AgCl electrode was used as reference electrode and a platinum foil was used as counter electrode. For minimizing the IR drop effect, the capillary bridge tip was very close to the surface of working electrode. The experiments were repeated for several times to ensure the reproducibility of the results saturated calomel electrode (SCE) as the reference electrode, a corrosive electrolyte (60 g/L NaCl) and an aluminum-copper sample with dimensions of 2.7 × 1.5 × 1.5 mm was used as a working electrode.

The potentiodynamic tests were carried out from -2.5 V to 2.5 V at a scan rate of 1 mV/s. Before the experiment, an immersion period of 30 minutes provided a reproducible homogeneous surface condition with a stable corrosion potential.

Scanning Kelvin Probe (SKP) measurements were performed using equipment from Princeton by the Versa scan software (USA). The microelectrode had a silver Pt/Ir tip with a diameter of approximately 10  $\mu\text{m}$  and vibrated with 30 $\mu\text{m}$  of amplitude, at an average distance of 100 $\mu\text{m}$  above the surface.

### **3. Results and Discussions**

The joint of dissimilar metals (0.95 Mg-Al-alloy and Pure Copper) made by Friction stir welding enhances the corrosion resistance properties and the key role is played by the tools travel speeds of weldment, such as 30mm/min, 40 mm/min, and 50 mm/min. The joint reflected the different morphology of the surface as shown in Figure 2. The full-welded view of 0.95 Mg-Al Alloy and Pure Copper samples by various tools travel speed (a) 30 mm/min, (b) 40mm/min, and (c) 50mm/min are shown respectively.

#### **3.1. Macrography Observation**

All the weldment is without any surface defects and with even appearance as can be seen in the figure. There is no flash formation during welding. Macrostructure and microstructure in the DXZ zone were formed due to various tool traveling speed such as 30,40, and 50 mm/min and are shown in Figure 3.

Figure 3 shows the information about the macro view of the three selected samples of constant tool rotational speed and varying tool travel speed such as 30 mm/min, 40 mm/min, and 50 mm/min. After observing the macrostructure of the weldment samples of cross-sectional region, the intermixing of the weld region shows a strong bonding between aluminum and copper. The materials flow in directional ways because of the threaded pin profiles giving the directional flowability of the materials.

Macroscopic aspect of fabricated welds are shown in Figure 4. Better intermixing of the aluminum-copper joint was observed at 40 mm/min, depending on the tool rotational speed, and traverse speed. And as compared to the other tool travel speed the 40 mm/min produces better surface

morphology. All the three welded plates are without any surface defects as shown in (Figure 2). Macro image of the weld zone showed no weld defects and micro structural steadiness was observed. There were micro structural dissimilarities with sites relative to the unaffected base metal. The weld area exhibited numerous micro structurally distinct regions including the DXZ zone along the weld center line, and the heat-affected zone (HAZ) adjacent to the stir zone as shown in Figure 4.

The base metal showed large deformation twins and slightly extended grain structures. Still, the extended grain structure vanished near the weld zone. The increase in the size of the grain was due to the annealing effect of welding heat. Very fine and equalized grain structure was seen in the central area of the weld zone. This may have occurred due to the recrystallization caused by the plastic shear deformation and frictional heat received simultaneously.

### **3.2. Micrography Observation**

Interpretation of microscopic examinations suggested that the process parameters have major impact on the formation of dissimilar aluminum-copper joints. Figure 4 shows the three different zones, the first one is heat affected zone (HAZ), second one is thermo-mechanical affected zone (TMAZ) and the third one is dynamic recrystallization zone (DXZ) or intermediate zone (IZ). The weldment is divided into two different sides such as advancing side (AS) and retreating side (RS). In this study Cu is located in advancing side and Al is located in retreating side. Microstructure of the joints fabricated by tapered threaded tool pin profile was studied using optical microscope to expose the quality of the stir zone. The microstructure of the samples with a tool traverse speed of 40 mm/min led to the development of coarser grains. This may be endorsed to higher heat input due to lower welding speeds that affects the coarsening of the grain size. The microstructure seen with the higher traverse speed of 50 mm/min displayed larger grains due to lower heat generation causing inadequate metal transportation, which results in deprived merging of the stirred material. The microstructure at the higher tool travel speed of 50 mm/min exposed a combination of coarse and fine grains.

The joints fabricated by tool rotation speed of 1350 rpm and weld speed of 40 mm/min produced joints without defects and with higher hardness. This may be attributed to the presence of smaller grains in the stir zone as compared to other conditions. The intense plastic deformation and frictional heat generation is observed due to the higher tool rotation speed and welding speed. FSW

produced the homogeneous grains with finer structure and that might have caused the enhancement in the properties.

The enlarged sight of the interface between the Al matrix and the Cu bulk is shown in Figure 4. Microstructure with full view of weldment and different zones such as heat affected zone (HAZ), thermomechanical affected zone (TMAZ), and dynamic recrystallization zone (DXZ) that is also called stir zone was observed in (Figure 4). During welding, the dynamic recrystallization occurred in complete welding zone because of sufficient heat generation and suitable parameters with threaded tool pin profile. The materials directional flowability and aluminum-copper joint both are face center cubic (FCC) materials, soft in nature but both having different melting points. If solidification time is more or uneven that can cause the formation of  $\text{CuAl}_2$ ,  $\text{CuAl}$ , and  $\text{Cu}_9\text{Al}_4$ . These are intermetallic phases that causes defect formation due to  $\text{Cu}_9\text{Al}_4$  which is very brittle in nature and  $\text{Cu}_9\text{Al}_4$  is formed in 350°- 410°C temperature range [16].

The higher tool rotational speed and lower tool traverse speed indicated the better deformations because of sufficient heat generation [17]. As can be observed from Figure 5a-b the aluminum-copper joint at 30 mm/min showed slight deformation of the grain size. In case of 50 mm/min tool travel speed the deformation is very less due to lack of heat generation as can be seen in Figure 5e-f. Whereas, for 40 mm/min the best deformation was seen due to the enough heat generation and proper fusion of aluminium and copper metals as is evident from Figure 5c-d. Grains and intermixing of the aluminum-copper is better at lower than higher tool travel speed. This is better parameter to get homogenous mixing of the aluminum-copper. Without deformed base metals microstructure is indication of the microstructural significance as shown in Figure 5g-h [18].

The picture of the interface among the Al and Cu is presented in Figure 6. The interface region of various tool travel speed by friction stir welding such as 30 mm/min with aluminum-copper microstructure is shown in Figure 6a, 40 mm/min is shown in Figure 6b and 50 mm/min is shown in Figure 6c. The Cu material adjacent to the area of the interface was plasticized due to the enough heat in the optimum range. Therefore, the fine discontinuous Cu particles were separated and dispersed in the stir zone. An interface exists among the Al matrix and the Cu bulk which is evident by the layered structure detected in the Cu bulk under the aluminum-copper interface.

### 3.3. Microhardness Examination

Mechanical properties of the joints investigated by various tool travel speed such as 30 mm/min, 40 mm/min, and 50 mm/min. of the FSW process are shown in Figure 8. It is observed that the joint fabricated by TT (tapered threaded) pin profile experienced superior properties with the joint efficiency of 78% compared to the other joints. The TT pin profile sweeps large amount of material from the plasticized zone [19]. The joint fabricated by 30 mm/min tool travel speed shows almost less tensile properties to compare of 40 mm/min tool travel speed. The friction heat generated by 30 mm/min tools travels speed might be smaller than that of 40 mm/min because the uneven heat generation and solidifying of the weldment of aluminum-copper joint is not suitable and formation of the intermetallic compounds and pin exerts an extra downward force. This is due to fine grain structure resulted in more ductile nature than all other joints. The microhardness that resulted from 50 mm/min tool travel speed are slightly lower compared to the 40 mm/min tool travel speed. The increase in heat generation and the formation of more intermetallic compounds at the aluminum-copper interface resulted in grains slightly bigger than the 40 mm/min tools travel speed. A clear nugget zone is observed which differs from the 30 mm/min specimen having low hardness. Moreover, the homogenous dissemination of Cu bulk in Al increased the mechanical properties of the 40 mm/min specimen. Microhardness survey was conceded on all the welded joints which are made by different tool travel speed [20]. The microhardness values compare to lower the base metals in different conditions with using different tool travels speed in details shown in Figure 8 their better hardness of the joint is under the process parameter conditions 40mm/min tool traverse speed and TT (tapered threaded tool pin profile).

### 3.4. Results obtained prior to corrosion tests

Figure 2 shows the patterns of XRD for selected three samples with base metals. The peaks of base alloy with different parameters of the travel speed such as 30 and 50 mm/min were identified as  $\text{Cu}_9\text{Al}_4$ ,  $\text{Al}_2\text{Cu}$ , Al, and Cu. The stirring behavior was observed at the weld center and finer grains were seen [1, 6].

The stirring action of the tool persuades high amount of plastic deformation and frictional heat generation between tool and BM. This is due to the mechanism of constant dynamic recrystallization zone (DXZ) [21]. The DXZ usually occurs in weld zone, and thus the microstructures can be refined. Small portions of TMAZ and HAZ were seen between WZ and

BM zone. A slightly elongated grain structure can be seen in the TMAZ zone due to the annealing effect of heat and severe plastic deformation of material around the pin edge [22]. Slightly coarse grains were seen in the HAZ zone located outside of the TMAZ zone which was affected only by the heat generation during the welding process[23]. DXZ is of great industrial interest due to the new grains being smaller than the initial grains that enhances the mechanical properties at room temperature.

### **3.5. Scanning Electron Microscopy (SEM) Examination After Corrosion Test**

Micro-pits generation on the welded surface and grain boundary cracking is observed after electrochemical tests on base metals alloy as shown in Figure 7. Essential intermetallic particles are also detected in the pitting areas. Previous research works have demonstrated that the intermetallic particles affect the corrosion of Al alloys [24-27]. The morphology of the intermetallic particles (i.e. spheroids, fiber-like or plate-like) is strongly affected by the applied cooling rate during solidification and its cathodic/anodic area ratio are closely related with the corrosion performance of different alloys [28, 29]. The increase in the number of particles cause the pitting and cracking in the WNZ and HAZ. Figure 7a shows a film generated by corrosion products with cracks that are not dense and are quite heterogeneous. These cracks could be correlated to the intergranular corrosion in the base alloy after the corrosion test. The HAZ region in the weld zone suffers more severe pitting corrosion compared to the base alloy for friction stir welding. Several small intergranular attacks are connected with the corroded surface of the HAZ. In the Figure 7b samples prepared at 40 mm/min tool travel speed showed no pit formation because of the better corrosion resistance properties of the joints. The figure shows the oxide layer during corrosion that is not severe as compared to the grain boundary cracking or pits formation.

Galvanic corrosion exists between the weld regions and the constituent particles, which have differences in chemical composition and microstructure. The cathodic process at the constituent particles induces alkalization [30, 31], that in turn leads to the dissolution of Al matrix. This may also attribute to the porous nature of the surface layer.

The corrosion properties for 50 mm/min tool travel speed are shown in 7c that are slightly higher as compared to the 40mm/min tool travel speed speed. The increase in heat generation and the formation of more intermetallic components at the aluminum-copper interface, causes enhanced

brittleness and reduction in tensile strength. As mentioned in previous literature [32], a decrease in the tensile strength of the joint happens with the increase in the thickness of the intermetallic phases.

### 3.6. Phase analysis of aluminum-copper welded samples after electrochemical tests

It is found that the XRD pattern of the aluminum-copper exactly matches with the peak shift for the Al and Cu metal [33]. The identified intermetallic formation on the interface region such as  $\text{Cu}_9\text{Al}_4$  and  $\text{CuAl}_2$  are found in the aluminum-copper weldment samples.

The X-ray diffraction analysis for the present phases and during welding formation of intermetallic can also be detected by the XRD analysis. 0.95 Mg-Al-alloy and pure copper samples were welded using different tools travel speed. The peak of the base metals and interface region of weldment at different process parameters such as (a) 0.95 Mg-Al-alloy (b) Pure Copper (c) 30 mm/min (d) 40 mm/min (e) 50 mm/min are shown in Figure 9. The XRD result clarified the present phases or phases formed during welding. Some specific intermetallic phases were formed such as  $\text{CuAl}$ ,  $\text{CuAl}_2$ , and  $\text{Cu}_9\text{Al}_4$  and remaining amount of  $\alpha$ -Al and Cu (saturated solid solution of Al in Cu) was also observed.

The present phases demonstrate that the weld of 0.95 Mg-Al-alloy to pure Cu involves the intermetallic compound such as  $\text{CuAl}_2$ ,  $\text{CuAl}$ , and  $\text{Cu}_9\text{Al}_4$  together with some of the  $\alpha$ -Al and Cu (saturated solid solution of Aluminum in Copper). The single phases of  $\alpha$ -Al and copper are identified near the 0.95 Mg-Al-alloy as well as near the dominant intermetallic compounds as shown in Figure 9c. As shown in Figure 9c no distinct  $\alpha$ -Al peak is found and intermetallic compound peaks correlate with the complex mixing of 0.95 Mg-Al-alloy and pure Cu grains in the weld zone. At tool travel speed of 40 mm/min as in Figure 9d XRD pattern shows the lack of intermetallics generation because of the sufficient heat generation and proper bonding between aluminum-copper.

According to the X-ray diffraction results, the high temperatures related with the strong stirring movement tool travel speed at 50 mm/min in Figure 9e cause the heterogeneous mixing of Al and Cu and results in the formation of intermetallic compounds  $\text{CuAl}_2$ ,  $\text{CuAl}$ , and  $\text{Cu}_9\text{Al}_4$ . The peaks of the face centered cubic copper structure with a wide composition range of aluminum is mainly

dispersed at the bottom of the weld nugget as can be seen in Figure 9. The ratios of aluminum over copper composition is sort to vary by 18.4 wt. % in the single phase of Cu.

The high temperature related with the strong stirring action tool travel speed cause the ununiformed mixing of aluminum-copper joint at 50 mm/min and results in the creation of intermetallic compounds CuAl, CuAl<sub>2</sub>, and Cu<sub>9</sub>Al<sub>4</sub>. Stronger CuAl<sub>2</sub> peaks than those of CuAl and Cu<sub>9</sub>Al<sub>4</sub> in the weld zone suggest an inadequate interaction time in spite of the strong stirring action of the tool pin [34].

A mixed layer of aluminum and copper that includes brittle intermetallic compounds such as CuAl<sub>2</sub>, CuAl, and Cu<sub>9</sub>Al<sub>4</sub> are formed that can be seen from the XRD outcomes and microstructural interpretations in the present dissimilar weld [35]. It is reflected that the softening of the stirred 0.95 Mg-Al-alloy enables the formation of the mixed layer and intermetallic compounds.

## 4. Electrochemical studies

### 4.1 Potentiodynamic Polarization studies

Polarization studies is globally used to observe instant corrosion rate of metal or an alloy exposed to a corrosive environment. Tafel plots were documented with in a range of -250 mV to +250 mV at the scan rate of 1 mV/s. The results were further quantitatively examined to obtain the Tafel slopes ( $\beta_a$  and  $-\beta_c$ ), the corrosion potentials ( $-E_{\text{corr}}$ ) and corrosion current density ( $I_{\text{cor}}$ ). The anodic current density ( $I_a$ ) can be expressed by equation and its log with  $b_a$  obtained by plotting  $\eta_{\text{reaction}}$  vs.  $\log I$ .

$$I_{\text{reaction}} = I_a = -I_o \exp\left(1 - \beta \frac{nF}{RT} \eta_{\text{reaction}}\right) \quad (1)$$

$$\eta_a = b_a \log_{10}\left(\frac{I_a}{I_o}\right) \quad (2)$$

$$b_a = 2.303 \frac{RT}{\beta nF} \quad (3)$$

Or,  $b_c = -(\beta nF / RT)$  and  $b_a = [(1 - \beta)nF / RT]$

where the number of electrons ( $n$ ) for an unknown reaction can be determined. The experiments were performed for 3.5wt % NaCl for 2 hours. The results are shown in Table 3.

Figure 10 shows polarization potentiodynamic graph for the three examined 30 mm/min, 40 mm/min, and 50 mm/min samples, which were performed in a stationary and aerated 3.5% sodium chloride solution at 22 ( $\pm 2$ ) °C.

The present investigation is focused on the effects of each intermetallics with respect to the matrix and the equivalent corrosion rate. After evaluating the three potentiodynamic polarization curves it can be assumed that the Al–Cu alloy displays corrosion of the Cu-rich phase and formation of copper oxide. This possibly initiates the mechanism of precipitation and dissolution of  $\text{AlCl}_2$ ,  $\text{Cu}(\text{OH})_4$ ,  $\text{CuO}$ , and  $\text{MgO}$  corrosion products. Considering the Al–Cu alloy sample, a partial steadiness is observed in the current density value of  $10.892 \mu\text{A cm}^{-2}$ . It is significant to note that the formation of Cu oxide becomes more stable near  $-578 \text{ mV (SCE)}$  [36]. Both the anodic and cathodic shifts can be observed from the potentiodynamic curves. The samples prepared with tool travel speed of 40 mm/min showed the best performance with lower corrosion current density value of  $14.776 \mu\text{A cm}^{-2}$  followed by 30 mm/min with  $18.205 \mu\text{A cm}^{-2}$  and 50 mm/min with  $24.232 \mu\text{A cm}^{-2}$  values. It should also be noted from Table 3 that base metal aluminum only showed less corrosion current density than the samples prepared with 40 mm/min tool travel speed [37]. The present current range used is to avoid the overloading of the instrument during the hot corrosion process at tool travel speed of 30 mm/min, 40 mm/min, and 50 mm/min.

#### 4.2. Electrochemical Impedance

After immersion of welded samples in 3.5% NaCl solution for one hour the Nyquist, bode and phase angle plots were obtained as shown in the Figure 11. It is identified that the impedance and phase angle increased with increase in the friction stir welding tool travel speed. The values of the various parameters after fitting the corresponding circuit is shown in the Table-6 In this equivalent circuit,  $R_s$  is the solution resistance,  $R_{ct}$  is the charge transfer resistance, and CPE is a constant phase element.

$$Z_{\text{CPE}} = R_s + \frac{R_{ct}}{1 + R_{ct} Y(j\omega)^n} \quad (4)$$

$$\left( j\omega \right)^n = \omega^n e^{j \frac{n\pi}{2}} = \omega^n \left( \cos \frac{n\pi}{2} + j \sin \frac{n\pi}{2} \right) \quad (5)$$

we can obtain the equation below after interpretation:

$$\left( Z' - R_s - \frac{R_{ct}}{2} \right)^2 + \left( -Z'' + R_{ct} \cot \frac{n\pi}{2} \right)^2 = \left( \frac{R_{ct}}{2} \csc \frac{n\pi}{2} \right)^2 \quad (6)$$

The depressed semicircle is represented by the above equation. The  $Z_{CPE}$ , of a CPE are expressed as

$$Z_{CPE} = \frac{1}{Y_0} [(j \omega)^n]^{-1} \quad (7)$$

where,  $Y_0$  remains the amplitude comparable to a capacitance,  $j$  be the square root of  $-1$ ,  $f_{max}$  is the AC frequency and  $n$  represents the phase shift. When  $n = 0$ , the CPE represents pure resistor, if  $n = +1$ , the CPE represents pure capacitor, and if  $n = -1$ , then CPE represents an inductor [38].

Figure 11a shows the Nyquist plots of the welded samples with different tool travel speed of 30 mm/min, 40 mm/min, and 50 mm/min in 3.5 wt. % of NaCl solution. The depressed semicircle can be seen for all the samples suggesting that the overall mechanism is not modified. The corrosion resistance was observed to be the best for sample welded with 40 mm/min tool travel speed. The diameter of the Nyquist plots can be seen to increase with increase in the charge transfer resistance ( $R_{ct}$ ) as shown in Table 4. The best resistance was shown at 1412 k $\Omega$  cm<sup>2</sup> followed by 986 k $\Omega$  cm<sup>2</sup> and 573 k $\Omega$  cm<sup>2</sup> respectively.

Figure 11b shows the bode plots of the samples welded with different tool travel speed of 30 mm/min, 40 mm/min and 50 mm/min. The slope values as obtained from the intermediate frequencies showed that as the corrosion resistance increases the values tend to move closer to 1. The closest value was obtained for 40 mm/min tool travel speed welded sample with 0.866, 0.820 for 30 mm/min welded sample and 0.744 for 50 mm/min welded sample as represented in Table 4.

Figure 11c shows the phase-angle plots for the welded samples in different frequency range. The phase angle plots are considered to move closer to 90° angle for good corrosion resistant surfaces. The best angle was observed at 64.2° approaching towards 90° for 40 mm/min tool travel speed. This was followed by 63.9° for 30 mm/min welded sample trailed by 61.3° for welded sample prepared with 50 mm/min tool travel speed as shown in Table 4.

### 4.3. Scanning Kelvin Probe (SKP)

SKP is one the most sophisticated methods available today to detect the localized corrosion on the metal surface. The probe vibrates over the working electrode surface creating a capacitor and an alternating current which flows between the probe and the working electrode [39]. Figure 12a represents the aluminum sample before corrosion and 12b shows the figure after corrosion. As can be observed from both the figures that the anodic activity is more in figure 12b after corrosion. The anodic potential is distributed all over the surface due to the corrosion and formation of pits. The similar case is observed for copper sample as shown in Figure 12c and 12d. The aggressive media attacked the surface and as a result the anodic potential are seen to dominate. Figure 12e and 12f represents the samples welded at 40 mm/min tool travel speed before and after corrosion. It is very clearly observed from Figure 12e that the sample is distinguished in aluminium, copper and intermetallic (welded) zone. This distinguished zone disappears as the corrosive solution attacks the surface leading to roughness, cracks and pits. More anodic potential is seen in case of corrosion or pits formation while cathodic potential is seen prior to corrosion suggesting that the surface is still intact and not corroded. These results support our previous results obtained from EIS and Tafel.

## 5. Conclusions

- (1) Three different tool travel speed of 30, 40 and 50 mm/min were used for friction stir welding of 0.95 Mg-Al-alloy and pure Cu specimens. The macrostructure study including SEM, and X-Ray diffraction analysis suggested that a decrease in the grain size from elongated to small and textural changes were the major effects caused by the increase in friction stir welding tool travel speed.
- (2) The potentiodynamic polarization suggestion a shift in anodic and cathodic regions. The corrosion current density was lowest for 40 mm/min welded samples suggesting its higher corrosion resistance properties in 3.5 wt. % of NaCl solution.
- (3) Electrochemical impedance suggested that the corrosion resistance of the welded sample prepared with 40 mm/min tool travel speed was the best as compared to others in 3.5 wt. % of NaCl solution. The charge transfer resistance, slope value, and phase angle values were found to be the best for 40 mm/min samples.
- (4) The resistance of corrosion mechanism of FSW samples can be related to the grain refinement and increase in homogeneity of microstructure which enhances the formation of corrosion resistant film on the welded samples. The homogenous distribution of the

impurities in the alloy by the friction stir welding, on which a homogenous passive film was observed that enhances the corrosion resistance of the samples.

### Conflicts of interest

Authors declare no conflicts of interest.

### Acknowledgements

The authors are thankful for the Sichuan 1000 Talent Fund and financial assistance provided by the X151517KCL42 open fund project.

## REFERENCES

- [1] Thomas, W. M.; Nicholas, E. D.; Needham, J. C.; Murch, M. G.; Temple S. P.; Dawes, C. J.; Improvements relating to friction stir welding. **1991** G.B. Patent No.9125978.8.
- [2] Stratton, S. W.; Circular of the bureau of standards, Copper wire tables, 13<sup>th</sup> edition, Washington, 1914.
- [3] Nam, N. D.; Dai, L. T.; Mathesh, M.; Bian, M. Z.; Thu, V. T. H.; Role of friction stir welding -Traveling speed in enhancing the corrosion resistance of aluminum alloy. *Mater Chem Phys* **2016**, *3*, 7-11.
- [4] Ghauri, F. A.; Deen, K. M.; Farooq, A.; Afzal, M.; Ahmad, A.; Evaluating the Electrochemical Behavior of Friction Stir-Welded AA2219-O Alloy Joint in 3.5% NaCl Solution. *JMEPEG* **2018**, *27*, 3429–3438.
- [5] Farhad Gharavi; Khamirul Amin Matoria; Robiah Yunus; Norinsan Kamil Othman; Firouz Fadaeifard; Corrosion behavior of Al6061 alloy weldment produced by friction stir welding process. *J. Mater. Res. Technol.* **2015**, *4*, 314–322.
- [6] Ouyang, J.; Reddy, E. Y.; Kovacevic, R.; Microstructural evolution in the friction stir welded 6061 aluminum alloy (T6-temper condition) to copper. *J. Mater. Process. Technol.* **2006**, *172*, 110–122.
- [7] Sare Celik; Recep Cakir; Effect of Friction Stir Welding Parameters on the Mechanical and Microstructure Properties of the Al-Cu Butt Joint. *Metals* **2016**, *6*, 133-147.

- [8] Staron, P.; Kocak, M.; Williams, S.; Wescott, A.; Residual Stress in Friction Stir-Welded Al Sheets, *Phys. B.* **2004**, *350*, 491–493.
- [9] Hatamleh, O.; Rivero, I. V.; Maredia, A.; Residual Stresses in Friction-Stir-Welded 2195 and 7075 Aluminum Alloys, *Metall. Mater. Trans. A.* 2008, *39*, 2867–2874.
- [10] Farajkhah, V.; Liu, Y.; Effect of Clamping Area and Welding Speed on the Friction Stir Welding-Induced Residual Stresses, *Int. J. Adv. Manuf. Technol.* **2017**, *90*,339–348.
- [11] Wadeson, D.; Zhou, X.; Thompson, G.; Skeldon, P.; Oosterkamp, L. D.; and Scamans, G.; Corrosion Behaviour of Friction Stir Welded AA7108 T79 Aluminium Alloy, *Corros. Sci.* **2006**, *48*, 887–897.
- [12] Kang, J.; Fu, R. D.; Luan, G. H.; Dong, C. L.; He, M.; In-Situ Investigation on the Pitting Corrosion Behavior of Friction Stir Welded Joint of AA2024-T3 Aluminium Alloy, *Corros. Sci.* **2010**, *52*, 620–626.
- [13] Jariyaboon, M.; Davenport, A.; Ambat, R.; Connolly, B.; Williams, S.; Price, D.; The Effect of Welding Parameters on the Corrosion Behaviour of Friction Stir Welded AA2024-T351, *Corros. Sci.* **2007**, *49*, 877–909.
- [14] Surekha, K.; Murty, B.; Rao, K. P.; Effect of Processing Parameters on the Corrosion Behaviour of Friction Stir Processed AA 2219 Aluminum Alloy, *Solid State Sci.* **2009**, *11*, 907–917.
- [15] Xu, W.; Liu, J.; Zhu, H.; Pitting Corrosion of Friction Stir Welded Aluminum Alloy Thick Plate in Alkaline Chloride Solution, *Electrochim. Acta.* **2010**, *55*, 2918–2923.
- [16] Birbilis, N.; Buchheit, R. G.; Investigation and Discussion of Characteristics for Intermetallic Phases Common to Aluminum Alloys as a Function of Solution pH, *J. Electrochem. Soc.* **2008**, *155*, 117-126.
- [17] M. Jafarzadegan, A. H. Feng, A. Abdollah-zadeh, T. Saeid, J. Shen, and H. Assadi, Microstructural characterization in dissimilar friction stir welding between 304 stainless steel and ST37 steel, *Mater. Charact.* **2012**, *74*, 28–41.
- [18] Suresh, M. V.; Vamshi Krishna B.; Rao, P.; Effect of pulse frequency in gas tungsten arc welding of powder metallurgical performs, *Sci Technol Weld Joi.* **2004**, *9*, 362-368.
- [19] Rodrigues, D. M.; Loureiro, A.; Leitao, C.; Leal, R. M.; Chaparro, B. M.; Vilaça, P.; Influence of friction stir welding parameters on the microstructural and mechanical properties of AA 6016-T4 thin welds, *Mater. Des.* **2009**, *30*, 1913–1921.

- [20] Kumar, A.; Raju, L. S.; Influence of Tool Pin Profiles on Friction Stir Welding of Copper, *Mater. Manuf. Process.* **2012**, *27*, 1414–1418.
- [21] Rao, C. V.; Reddy, G. M.; Rao, K. S.; Microstructure and Pitting Corrosion Resistance of AA2219 Al-Cu Alloy Friction Stir Welds- effect of Tool Profile, *Def. Technol.* **2015**, *11*, 123–131.
- [22] Devaraju, A.; Influence of Post-weld Rapid cooling on Grain size and Mechanical properties of Friction Stir Welded AA 2014, *Mater. Today Proc.* **2017**, *4*, 3722–3727.
- [23] Farhad Gharavi, Khamirul Amin Matori, Robiah Yunus, Norinsan Kamil Othman, Investigation of the Nugget Zone Corrosion Behavior in Friction Stir Welded Lap Joints of 6061-T6 Aluminum Alloy, *Mat. Res.* **2014**, *17*, 1563-1574.
- [24] Zucchi, F.; Trabanelli, G.; Grassi, V.; Pitting and stress corrosion cracking resistance of friction stir welded AA5083, *Mater. Corros.* **2001**, *52*, 853–859.
- [25] Trueba, M.; Trasatti, S. P.; Study of Al alloy corrosion in neutral NaCl by the pitting scan technique, *Mater. Chem. Phys.* **2010**, *121*, 523–533.
- [26] Zaid, B.; Saidi, D.; Benzaid, A.; Hadji, S.; Effects of pH and chloride concentration on pitting corrosion of AA6061 aluminum alloy, *Corros. Sci.* **2008**, *50*, 1841–1847.
- [27] Osorio, W. R.; Garcia, L. R.; Peixoto, L. C.; Garcia, A.; Electrochemical behavior of a lead-free snag solder alloy affected by the microstructure array, *Mater. Des.* **2011**, *32*, 4763–4772.
- [28] Osorio, W. R.; Freire, C. M.; Caram, R.; Garcia, A.; The role of Cu-based intermetallics on the pitting corrosion behavior of Sn–Cu, Ti–Cu and Al–Cu alloys, *Electrochim. Acta.* **2012**, *77*, 189–197.
- [29] Ezuber, H.; Houd, El. A.; Shawesh, El. F.; A study on the corrosion behaviour of aluminium alloys in seawater, *Mater. Des.* **2008**, *29*, 801-805.
- [30] Park, J. O.; Paik, C. H.; Huang, Y. H.; Alkire, R. C.; Influence of Fe-rich intermetallic inclusions on pit initiation on aluminium alloys in aerated NaCl, *J Electro. Chem. Soc.* **1999**, *146*, 517–523.
- [31] Rodrigues, D. M.; Loureiro, A.; Leitao, C.; Leal, R. M.; Chaparro, B. M.; Vilaça, P.; Influence of friction stir welding parameters on the microstructural and mechanical properties of AA 6016-T4 thin welds, *Mater. Des.* **2009**, *30*, 1913–1921.

- [32] Ayyagari, Aditya V.; Gwalani, Bharat; Muskeri, Saideep; Mukherjee Sundeep; Banerjee, Rajarshi; Surface degradation mechanisms in precipitation-hardened high-entropy alloys, *Mater. Degrad.* **2018**, *2*, 1-10.
- [33] Xue, P.; Ni, D. R.; Wang, D.; Xiao, B. L.; Ma, Z. Y.; Effect of friction stir welding parameters on the microstructure and mechanical properties of the dissimilar Al–Cu joints, *Mater. Sci. Eng. C.* **2011**, *528*, 4683–4689.
- [34] Kumar, A.; Sunderrajan, S.; Effect of welding parameters on mechanical properties and optimization of pulsed TIG welding of Al-Mg-Si alloy, *Int. J. Adv. Manuf. Technol.* **2008**, *42*, 118-125.
- [35] Suresh, M. V.; Vamshi Krishna B.; and Rao, Prasad; Effect of pulse frequency in gas tungsten arc welding of powder metallurgical performs, *Sci Technol Weld Joi.* **2004**, *9*, 362-368.
- [36] Rajkumar, S.; Muralidharan C.; and Balasubramanian, V.; Influence of friction stir welding process and tool parameters on strength properties of AA7075-T6 aluminium alloy joints, *Mater. Des.* **2011**, *32*, 535-549.
- [37] Zhang, X. L.; Jiang, Zh. H.; Yao, Zh. P.; Song, Y.; Wu, Zh. D.; Effects of scan rate on the potentiodynamic polarization curve obtained to determine the Tafel slopes and corrosion current density, *Corros. Sci.* **2009**, *51*, 581-587.
- [38] Dileep Kumar Yadav; Mumtaz Ahmad Quraishi; Application of Some Condensed Uracils as Corrosion Inhibitors for Mild Steel: Gravimetric, Electrochemical, Surface Morphological, UV–Visible, and Theoretical Investigations, *Ind. Eng. Chem. Res.* **2012**, *51*, 14966–14979.
- [39] Hongwei Feng; Ambrish Singh; Yuanpeng Wu; Yuanhua Lin; SECM/SKP and SVET studies on mitigation of N80 steel corrosion by some polymers, *New. J. Chem.* **2018**, *42*, 11404-11416.

## Figure Captions:

**Figure 1.** Pattern followed for micro-hardness test using Vickers digital machine.

**Figure 2.** Surface morphology of full-welded zones of 0.95 Mg-Al-alloys and Pure Copper samples by various tools travel speed (a) 30 mm/min, (b) 40 mm/min, and (c) 50 mm/min.

**Figure 3.** Macrostructure of full-welded zones of 0.95 Mg-Al-alloys and Pure Copper samples by various tools travel speed (a) 30 mm/min, (b) 40 mm/min, and (c) 50 mm/min.

**Figure 4.** Macro with microstructure view of different zones of Aluminum-Copper welded sample with using 1350rpm and 40 mm/min process parameters.

**Figure 5.** Microstructure view of after and before welded with of Pure Copper (left side) and 0.95 Mg-Al alloy (right side) samples by various tools travel speed (a-b) 30mm/min, (c-d) 40mm/min, (e-f) 50mm/min, and (g-h) BM alloy.

**Figure 6.1** Microstructure of stir zone (SZ) of FSW joints at various conditions of Aluminum-Copper (a) 30 mm/min (c) 40 mm/min (e) 50 mm/min.

**Figure 7.** SEM analysis samples after electrochemical tests showing micro pits on the exposed area of the samples (a) 30 mm/min (b) 40 mm/min (c) 50 mm/min (d) Pure Copper (e) 0.95 Mg-Al-Alloy.

**Figure 8.** Microhardness distribution of FSW joints for different tool travels speed and base metal (Aluminum-Copper) advance side Copper and retreating side Aluminum.

**Figure 9.** 2 XRD plot showing the peak of the base metals and interface region of weldment at different process parameters. (a) 0.95 Mg-Al-alloy (b) Pure Copper (c) 30 mm/min (d) 40 mm/min (e) 50 mm/min.

**Figure 10.** Potentiodynamic Polarization curves in 3.5wt. % NaCl solution at  $22^{\circ} \pm 0.5^{\circ} \text{C}$  for (a) Base Metals (b) Welded samples of different tool travel speed 30,50, and 40mm/min respectively.

**Figure 11.** Electrochemical spectrum of samples with and without deformation (a-b) Nyquist (c-d) Bode plots and (e-f) Phase angle plots.

**Figure 12.** SKP spectrum of samples before and after corrosion (a) 2D and 3D figure of pure Al (b) 2d and 3D figure of pure Al after corrosion (c) 2D and 3D figure of pure Cu (d) 2d and 3D figure of pure Cu after corrosion (e) 2D and 3D figure of welded sample at 40 mm/min (f) 2D and 3D figure of welded sample at 40 mm/min after corrosion.

## **Table Captions:**

**Table 1.** Chemical composition of base metals (Wt. %).

**Table 1.** Chemical composition of AISI-H13 tool steel (Wt. %).

**Table 3.** Aluminum-Copper in 3.5wt% NaCl for 2hr time with Different conditions and constant tool pin profile.

**Table 4.** Impedance data for Aluminum-Copper in 3.5 wt. % NaCl at various tool travel speed conditions.

**Table 1.** Chemical composition of base metals (Wt. %).

Pure Copper	Zn	Al	Si	Sn	P	S	Pb	Fe	Cu
	0.005	0.005	0.005	0.007	0.001	0.013	0.01	0.04	Bal.
0.95 Mg-Al-alloy	Cu	Zn	Si	Ti	Mg	Mn	Cr	Fe	Al
	0.2	0.013	0.066	0.017	0.95	0.11	0.12	0.27	Bal.

**Table 2.** Chemical composition of AISI-H13 tool steel (Wt. %).

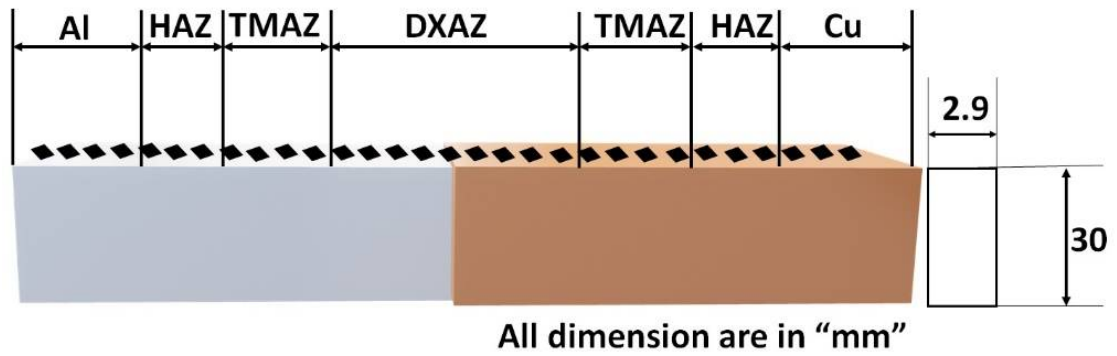
Element	C	Mn	P	S	Si	Cr	V	Mo
Amount (Wt %)	0.42	0.28	0.015	0.003	1	5.2	1.05	1.45

**Table 3.** Aluminum-Copper in 3.5wt% NaCl for 2hr time with Different conditions and constant tool pin profile.

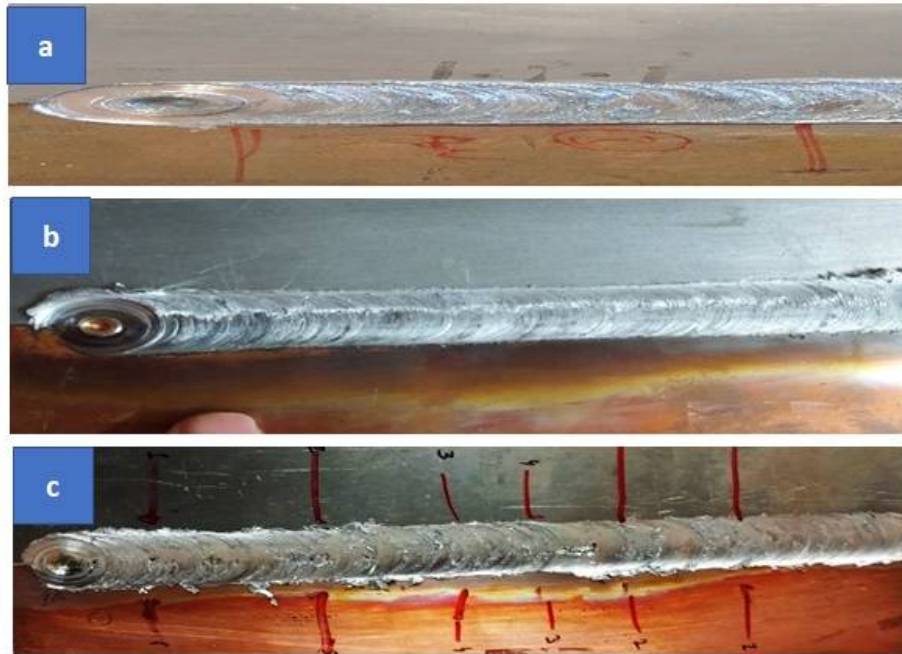
Sample Condition	Cathodic $\beta(mV)$	Anodic $\beta(mV)$	$E_{corr}(mV)$	$I_{corr}(\mu A)$
BM/Copper	317.833	93.368	-214.441	16.208
BM/Aluminum	630.396	29.834	-644.800	10.892
30 mm/min	475.846	25.278	-638.644	18.205
40 mm/min	469.029	54.738	-578.039	14.776
50 mm/min	637.031	33.529	-656.799	24.232

**Table 4.** Impedance data for Aluminum-Copper in 3.5 wt. % NaCl at various tool travel speed conditions.

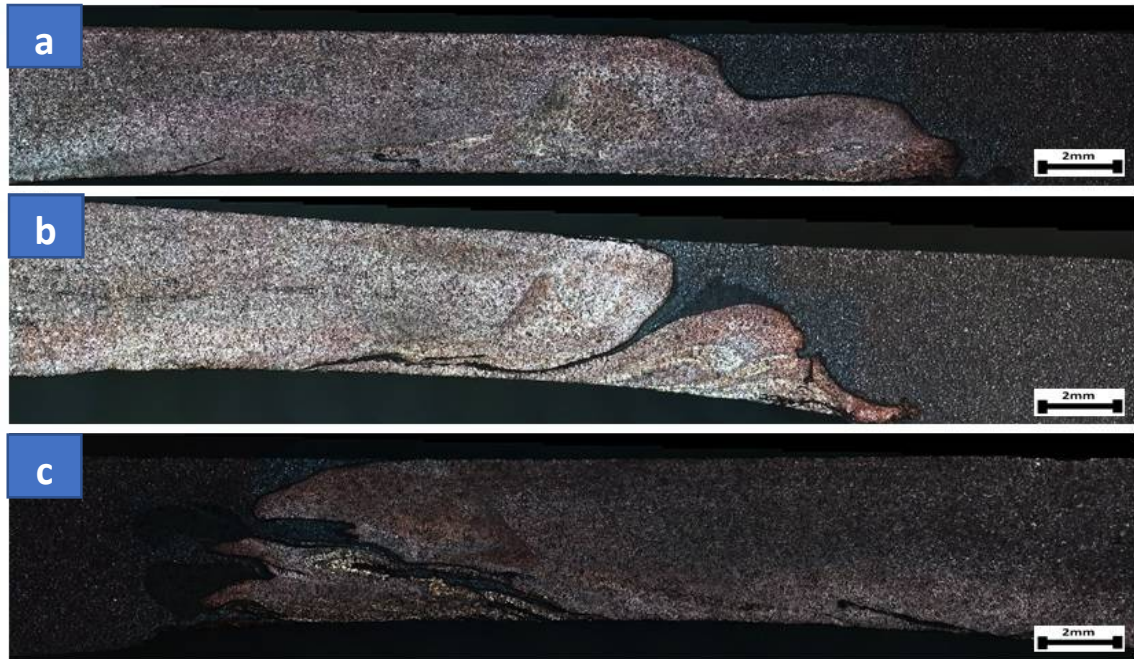
<b>Samples</b>	<b><math>R_s</math></b> (ohm cm <sup>2</sup> )	<b>CPE</b> <b>S.sn.cm<sup>-2</sup></b>	<b>n</b>	<b><math>R_{ct}</math></b> (ohm cm <sup>2</sup> )	<b>-S</b>	<b><math>\alpha</math> (°)</b>
0.95 Mg-Al-alloy	27.71	0.000432	0.837	375.5	0.912	52.4
Copper	5.451	0.000957	0.735	179	0.859	46.7
30 mm/min	4.631	0.000639	0.856	986	0.82	63.9
40 mm/min	2.708	0.000932	0.848	1412	0.866	64.2
50 mm/min	5.242	0.000402	0.799	573	0.744	61.3



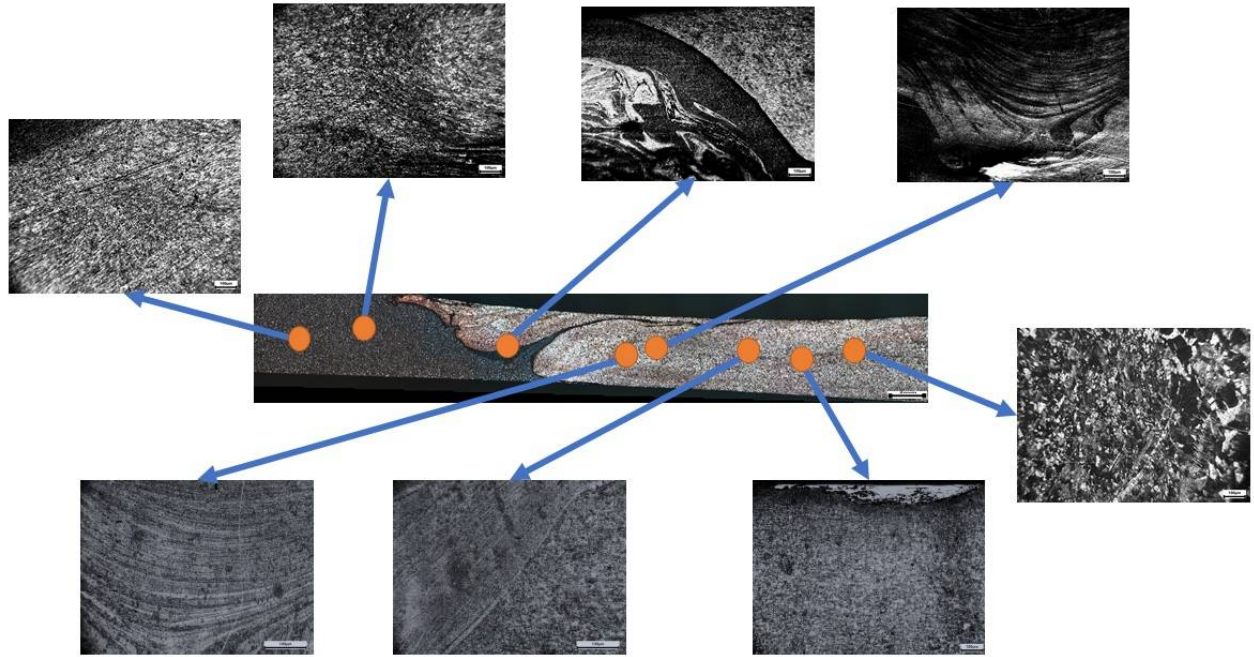
**Figure 1.** Pattern followed for micro-hardness test using Vickers digital machine.



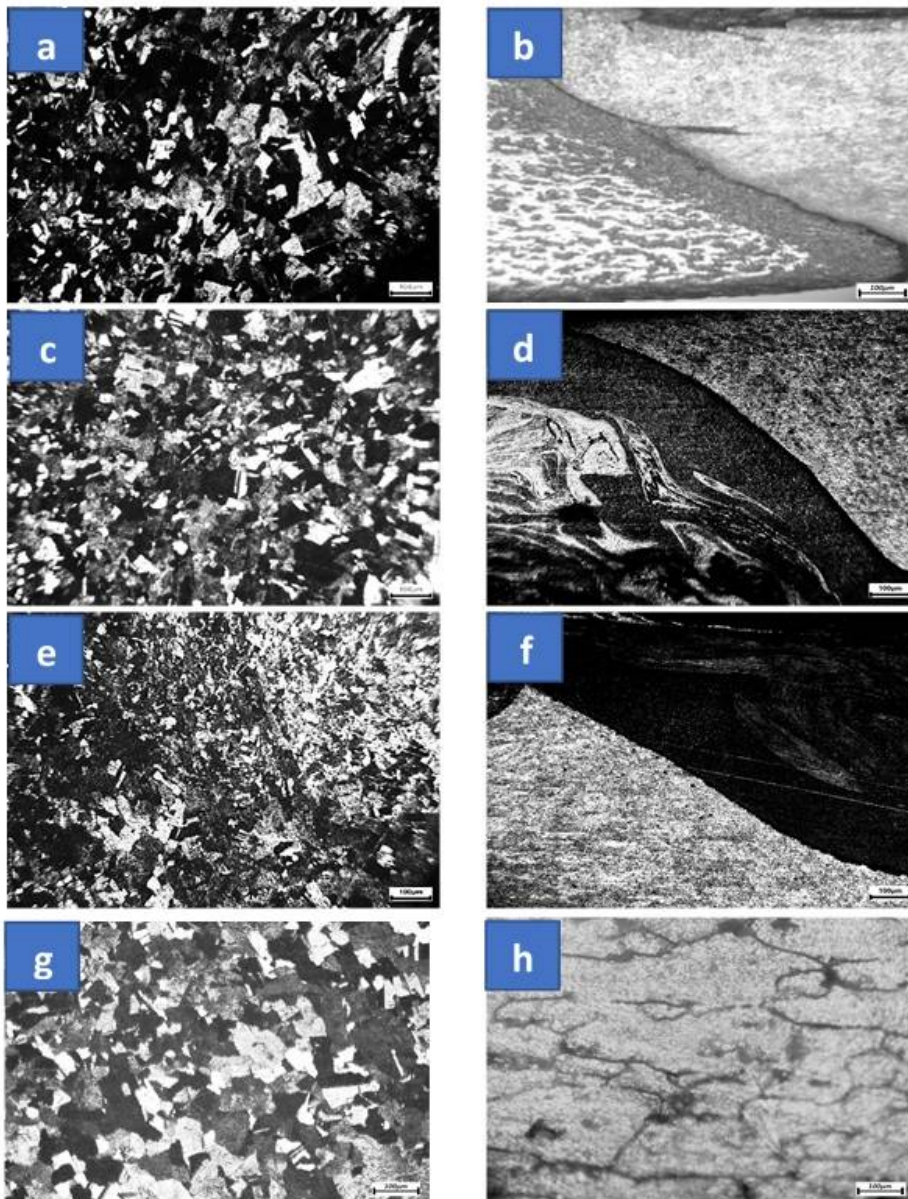
**Figure 2.** Surface morphology of full-welded zones of 0.95 Mg-Al-alloys and Pure Copper samples by various tools travel speed (a) 30 mm/min, (b) 40 mm/min, and (c) 50 mm/min.



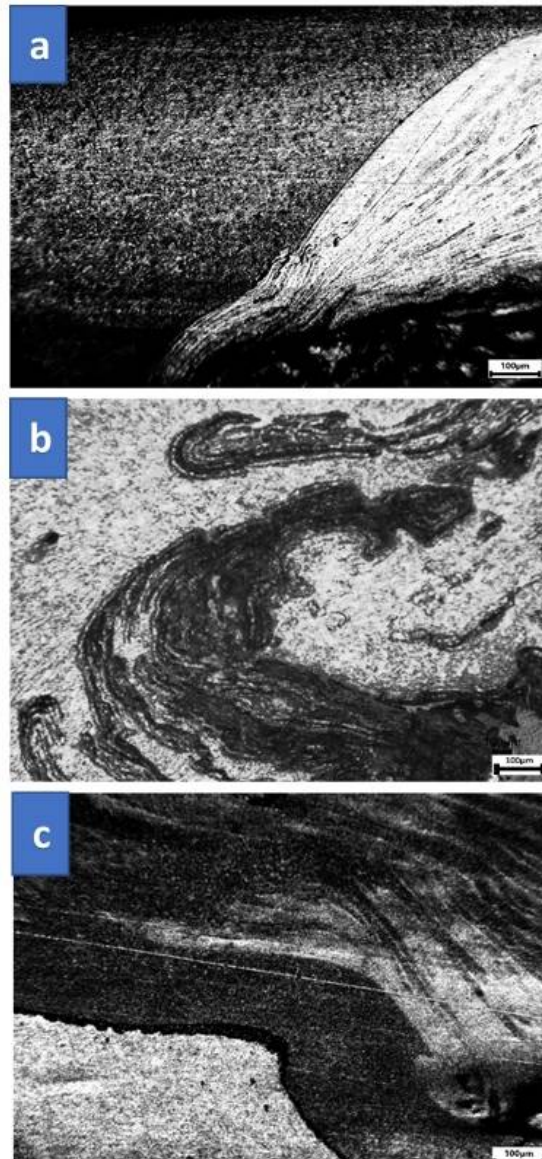
**Figure 3.** Macrostructure of full-welded zones of 0.95 Mg-Al-alloys and Pure Copper samples by various tools travel speed (a) 30 mm/min, (b) 40 mm/min, and (c) 50 mm/min.



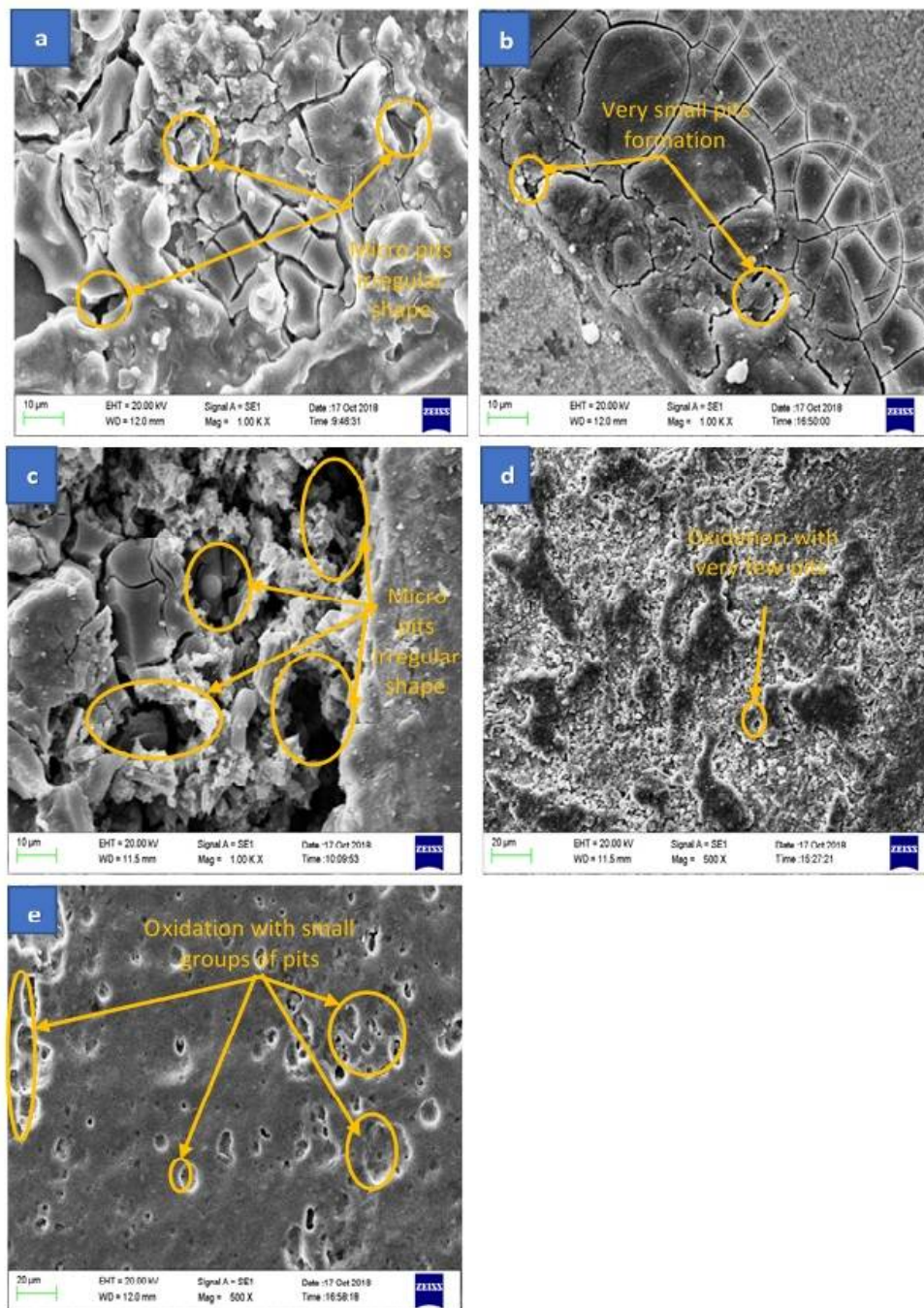
**Figure 4.** Macro with microstructure view of different zones of Aluminum-Copper welded sample with using 1350rpm and 40 mm/min process parameters.



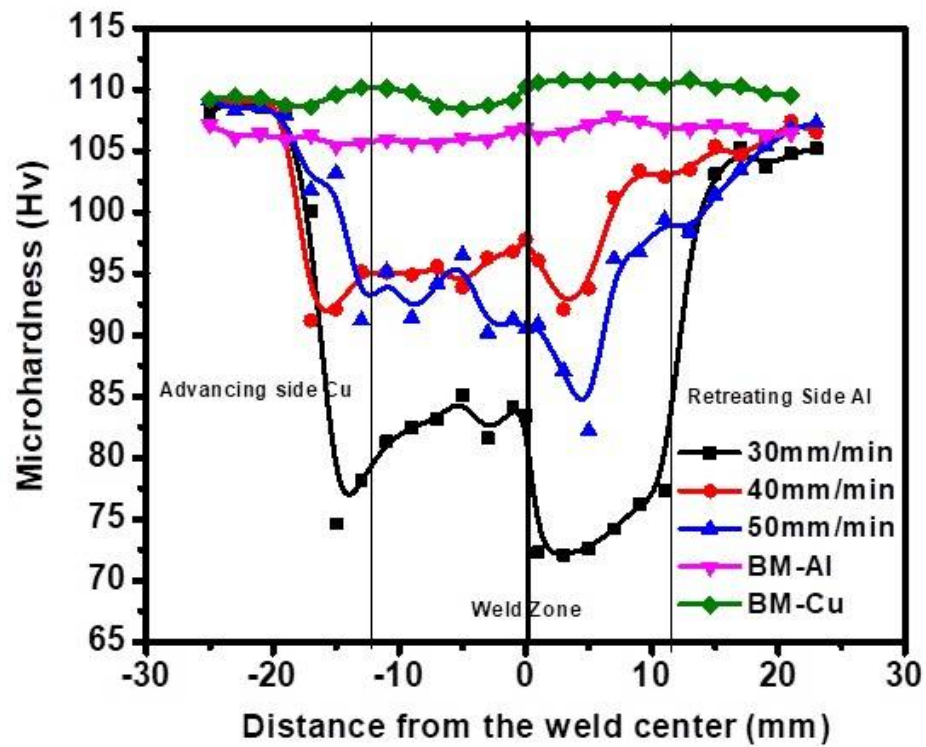
**Figure 5.** Microstructure view of after and before welded with of Pure Copper (left side) and 0.95 Mg-Al alloy (right side) samples by various tools travel speed (a-b) 30mm/min, (c-d) 40mm/min, (e-f) 50mm/min, and (g-h) BM alloy.



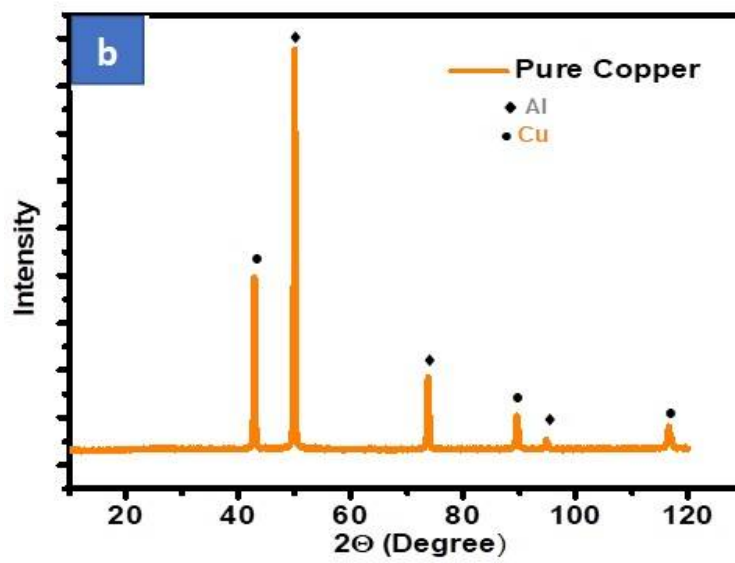
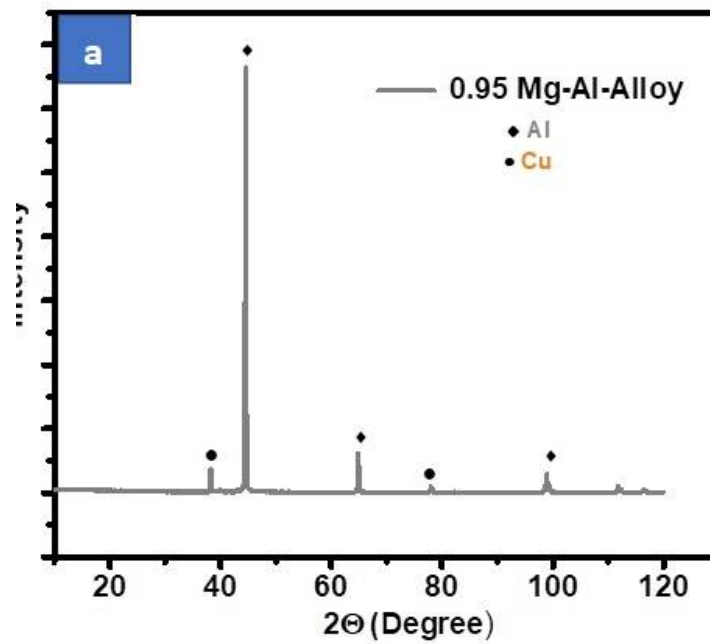
**Figure 6.3** Microstructure of stir zone (SZ) of FSW joints at various conditions of Aluminum-Copper (a) 30 mm/min (c) 40 mm/min (e) 50 mm/min.

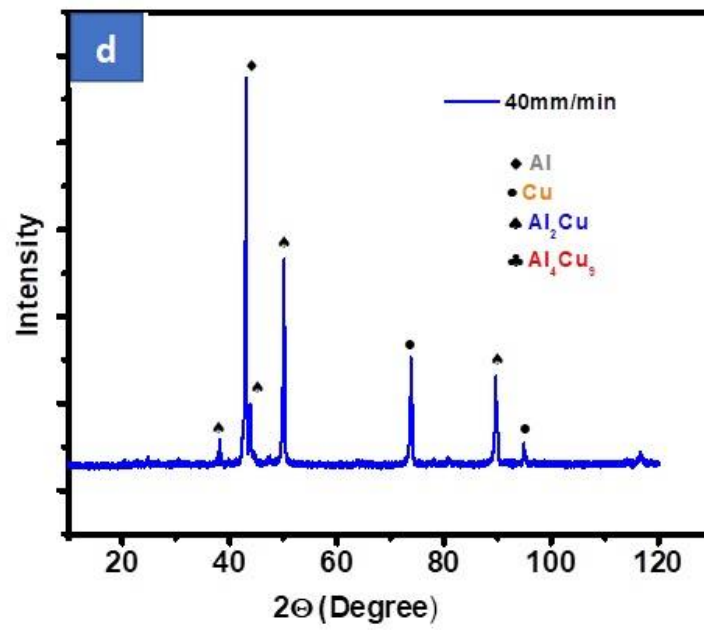
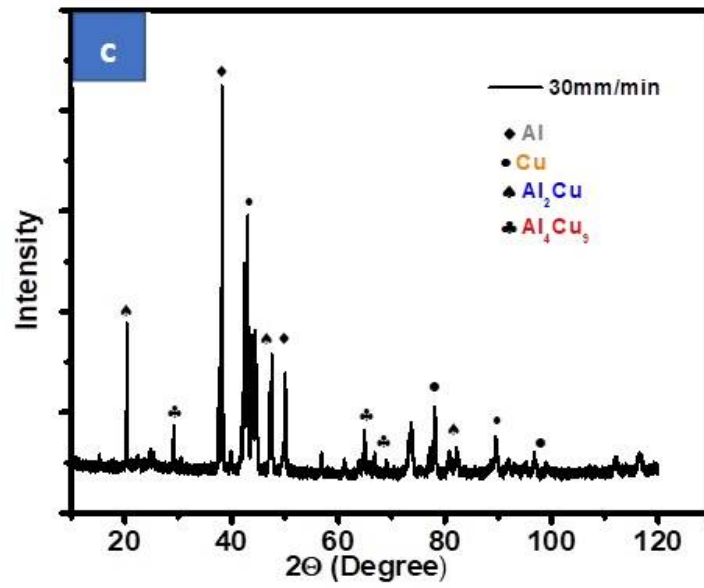


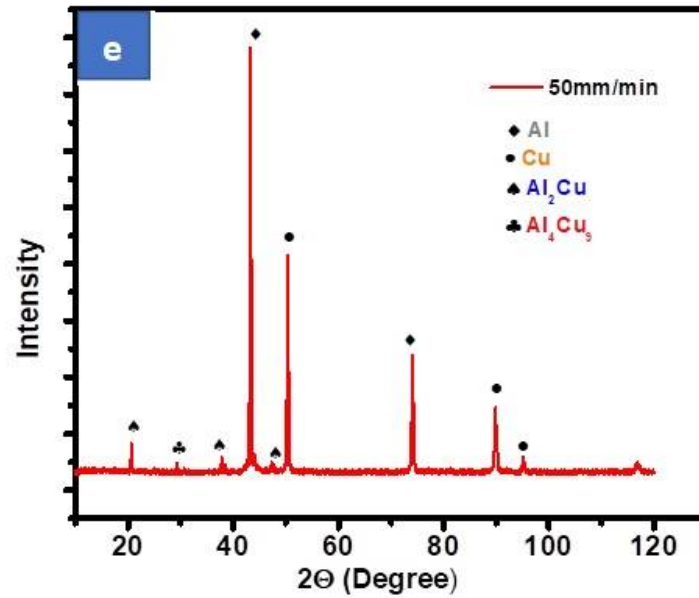
**Figure 7.** SEM analysis samples after electrochemical tests showing micro pits on the exposed area of the samples (a) 30 mm/min (b) 40 mm/min (c) 50 mm/min (d) Pure Copper (e) 0.95 Mg-Al-Alloy.



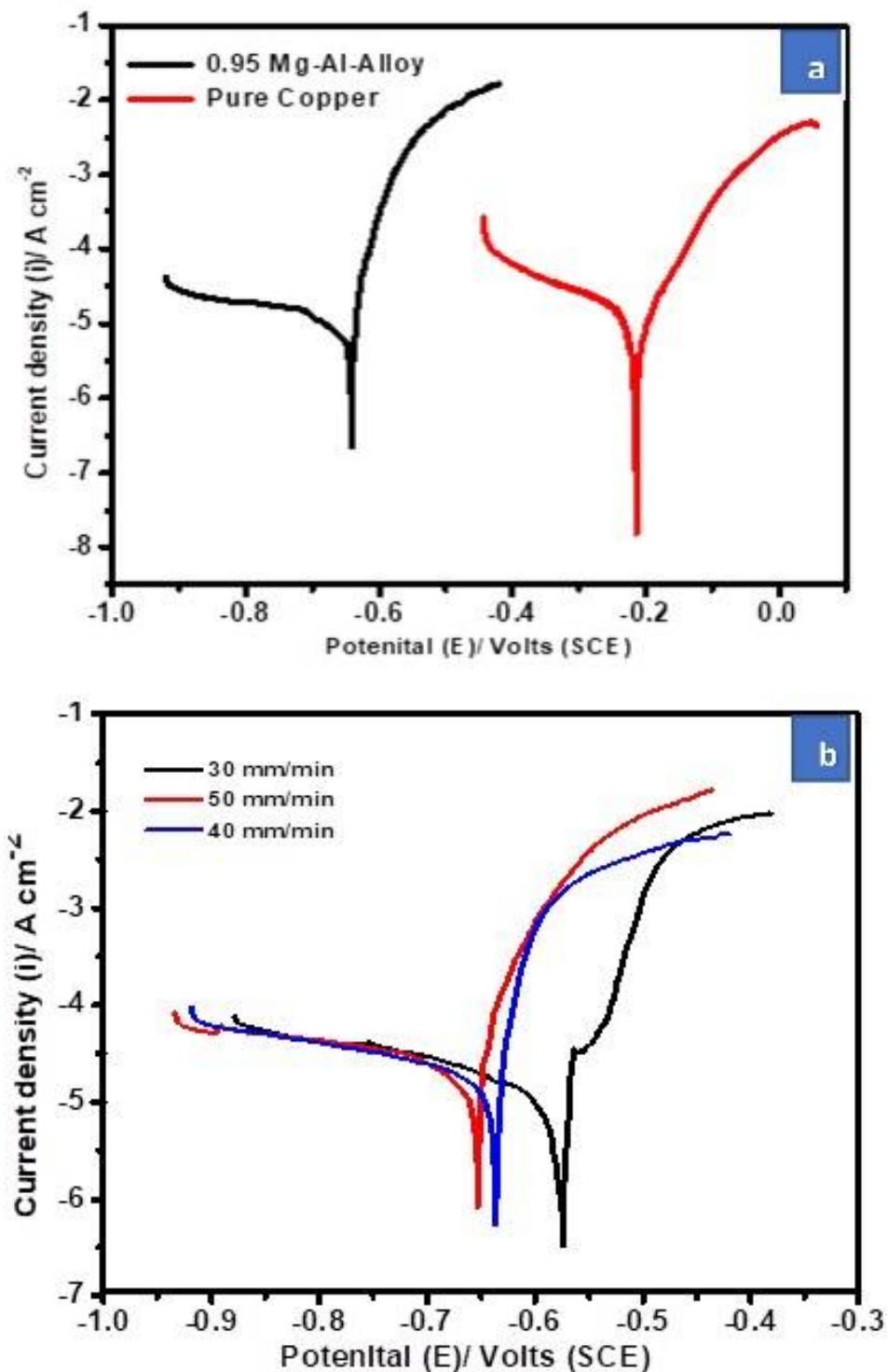
**Figure 8.** Microhardness distribution of FSW joints for different tool travels speed and base metal (Aluminum-Copper) advance side Copper and retreating side Aluminum.



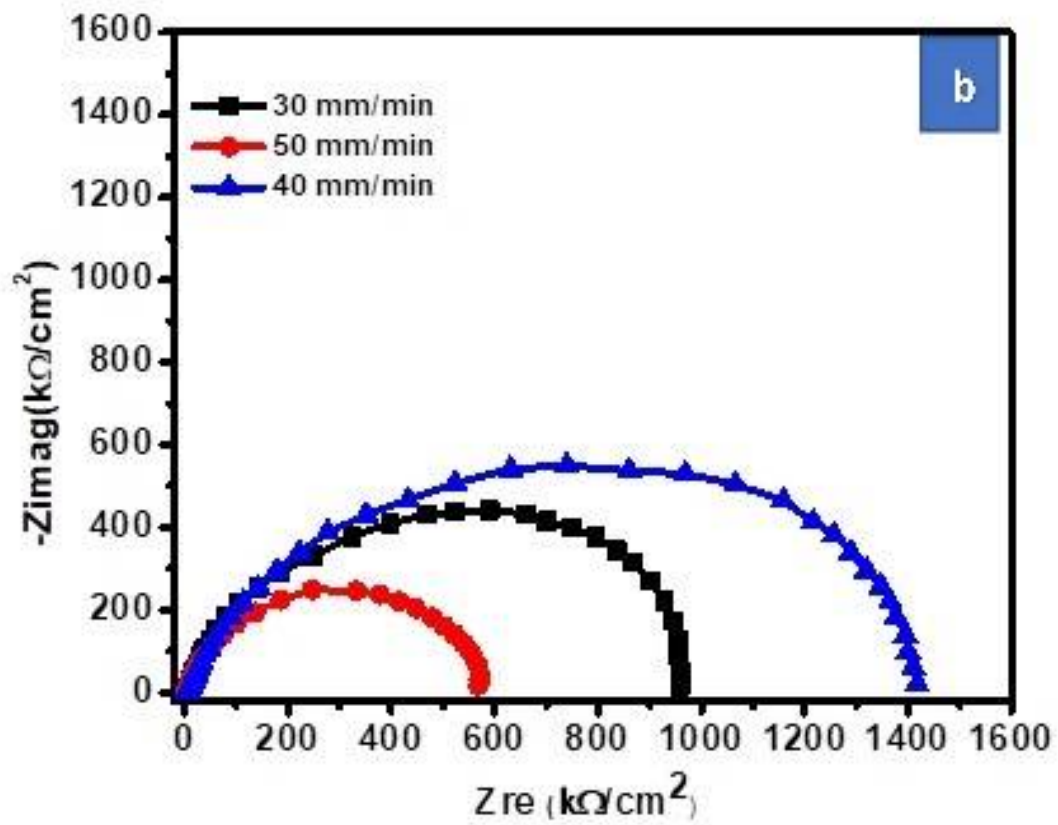
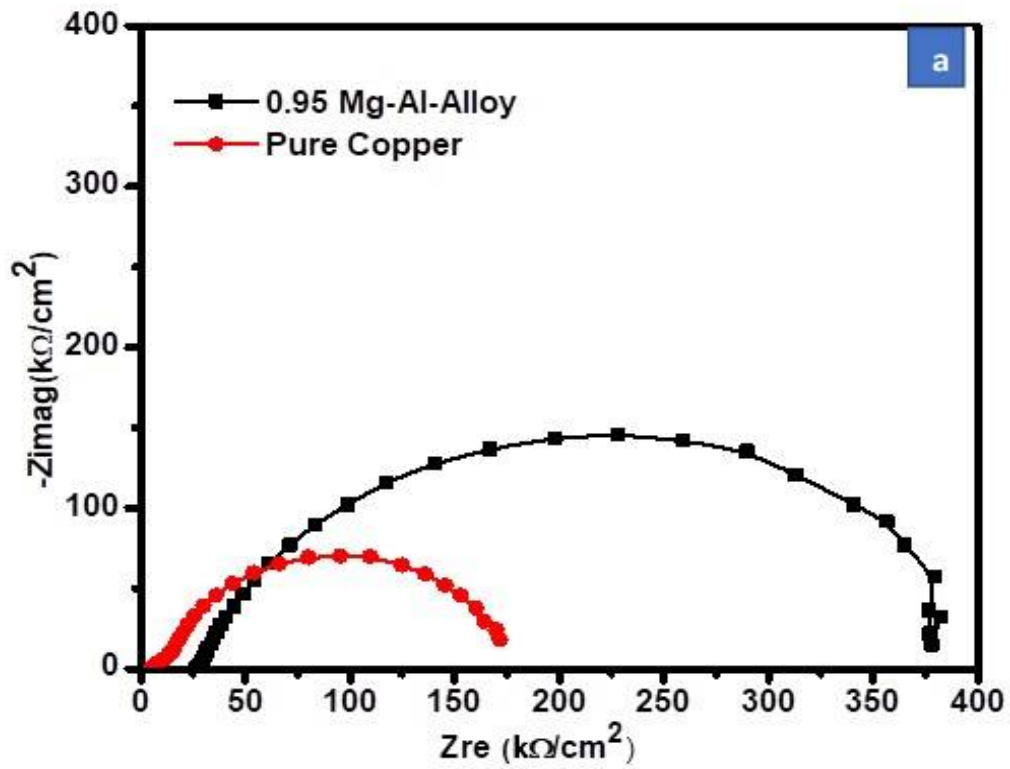


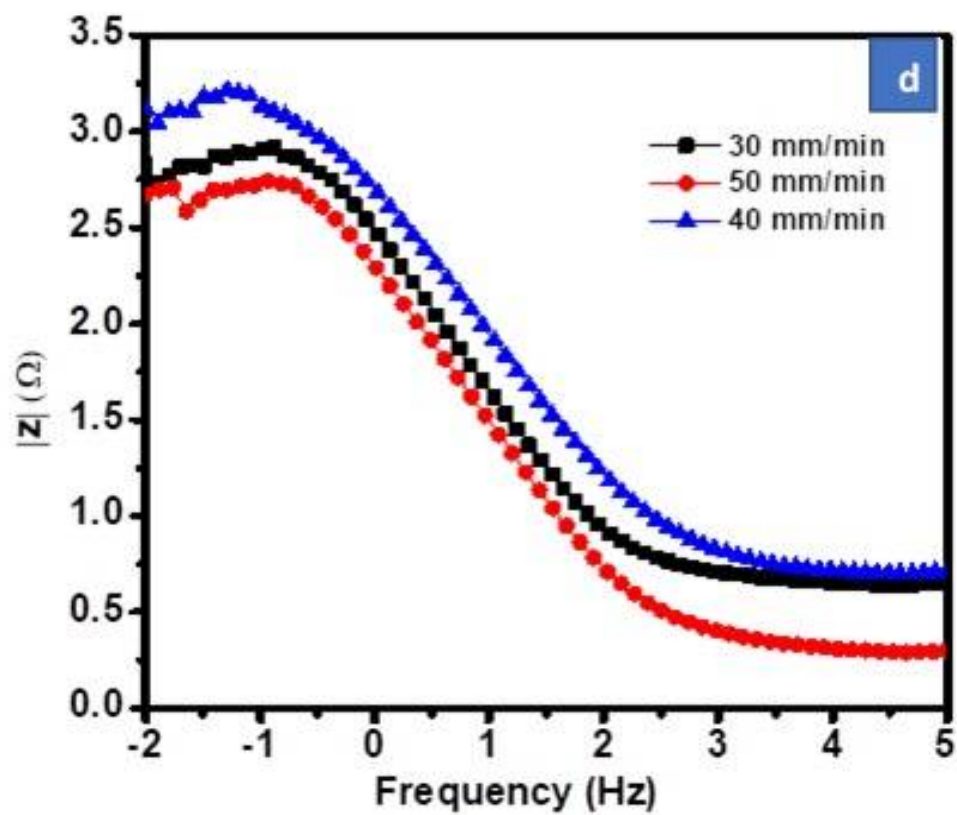
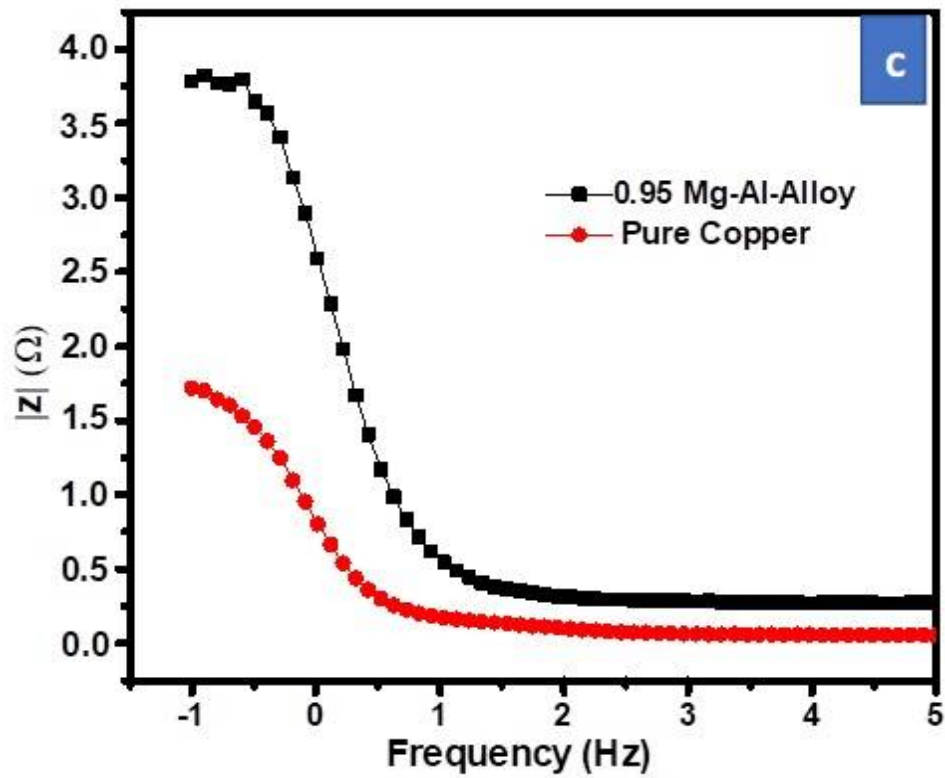


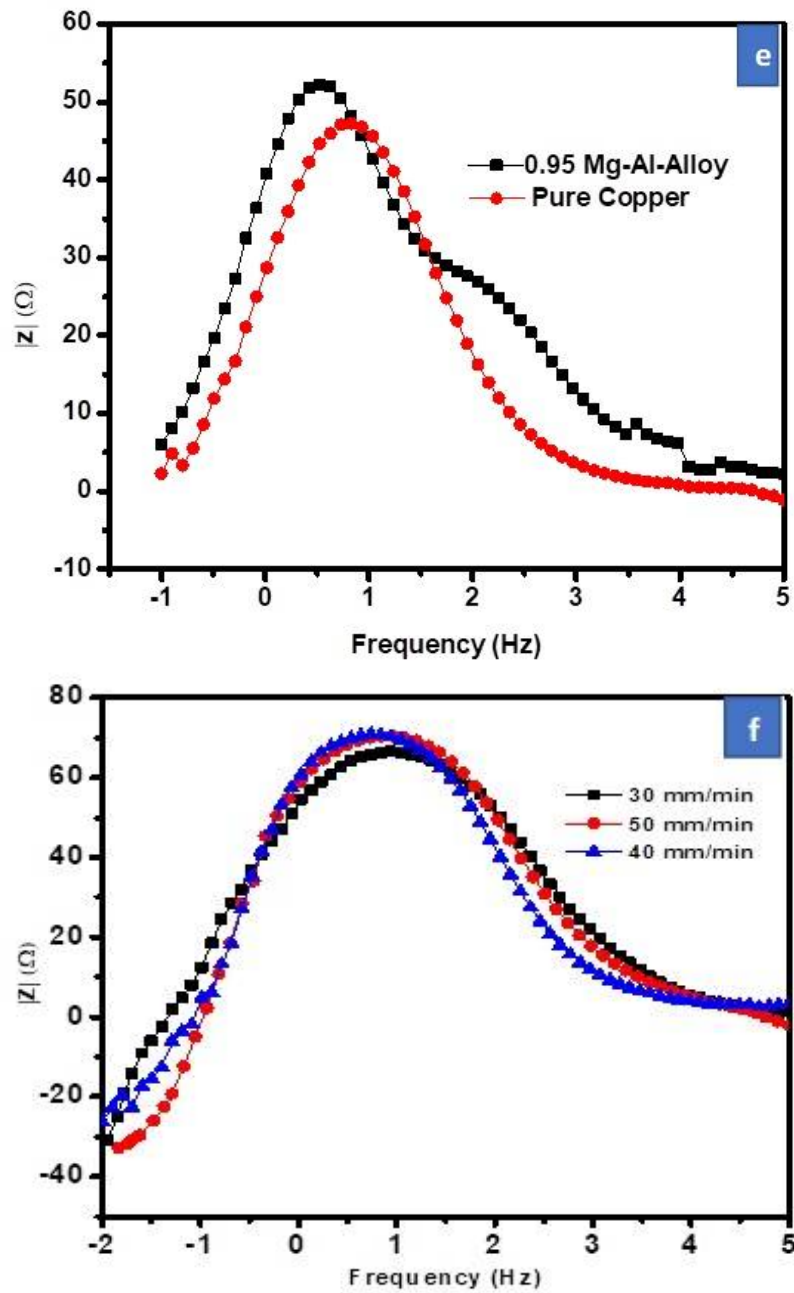
**Figure 9. 4** XRD plot showing the peak of the base metals and interface region of weldment at different process parameters. (a) 0.95 Mg-Al-alloy (b) Pure Copper (c) 30 mm/min (d) 40 mm/min (e) 50 mm/min.



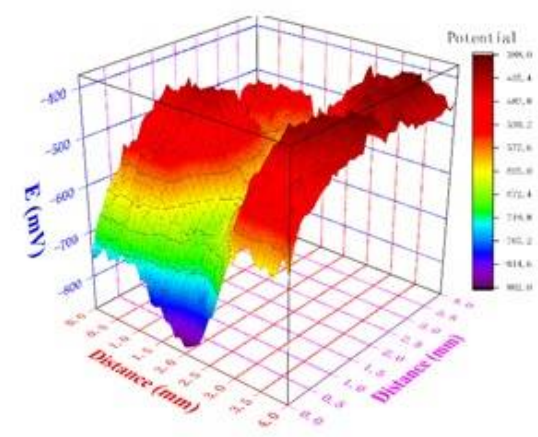
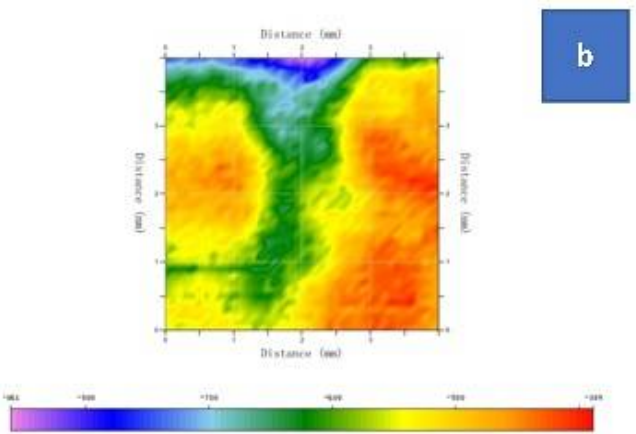
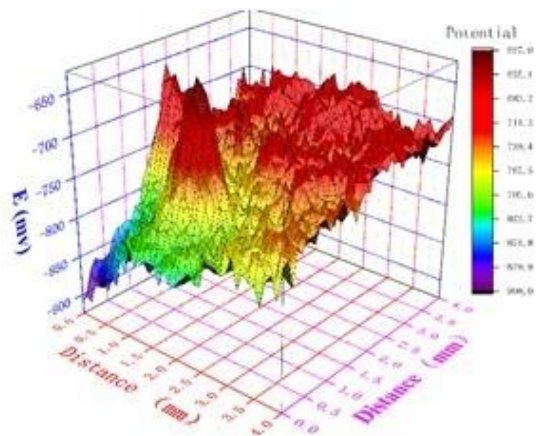
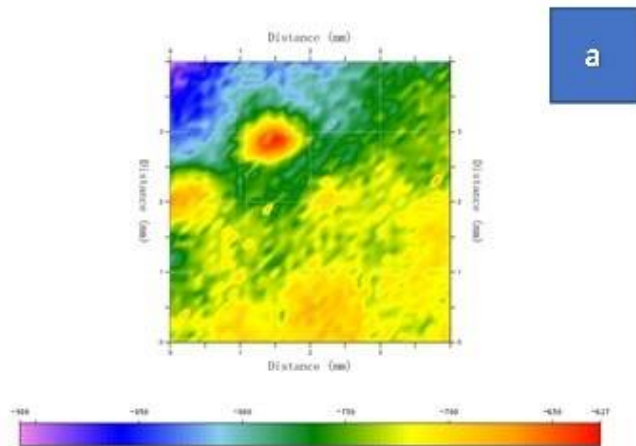
**Figure 10.** Potentiodynamic Polarization curves in 3.5wt. % NaCl solution at  $22^{\circ} \pm 0.5^{\circ} \text{C}$  for (a) Base Metals (b) Welded samples of different tool travel speed 30,50, and 40mm/min respectively.

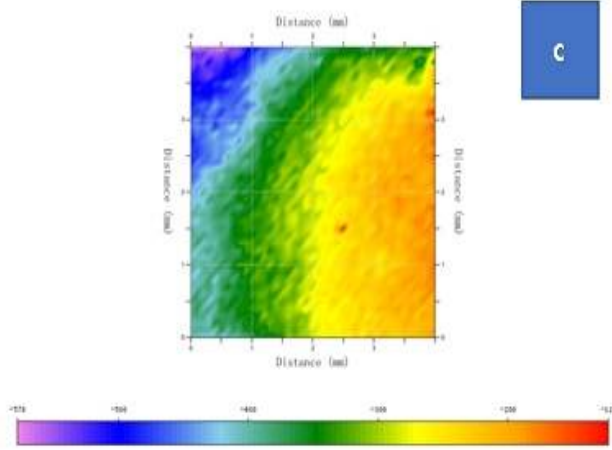




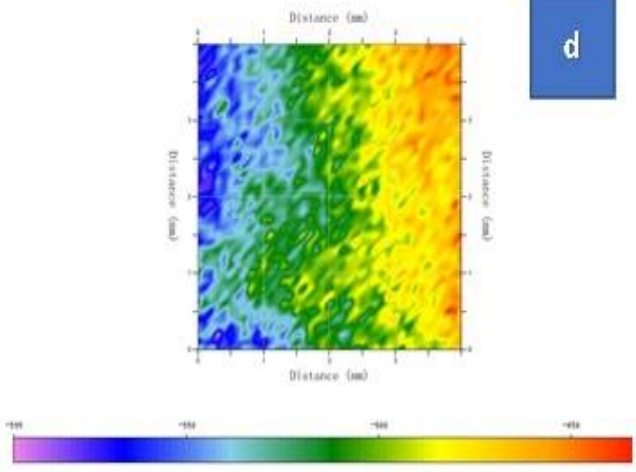
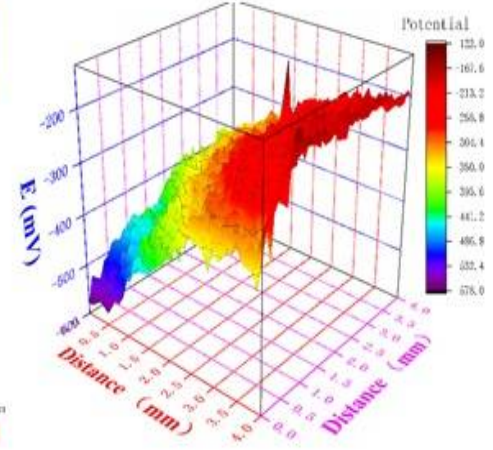


**Figure 11.** Electrochemical spectrum of samples with and without deformation (a-b) Nyquist (c-d) Bode plots and (e-f) Phase angle plots.

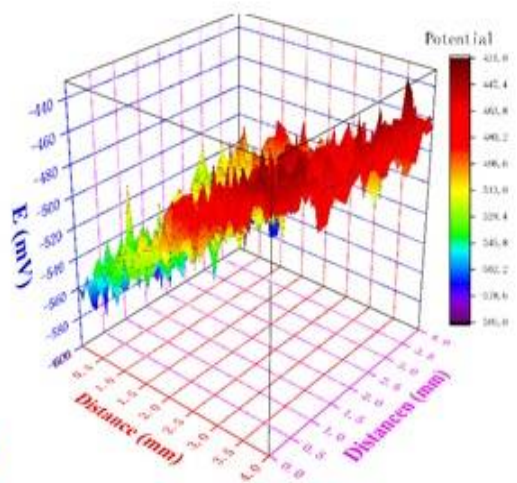




c



d



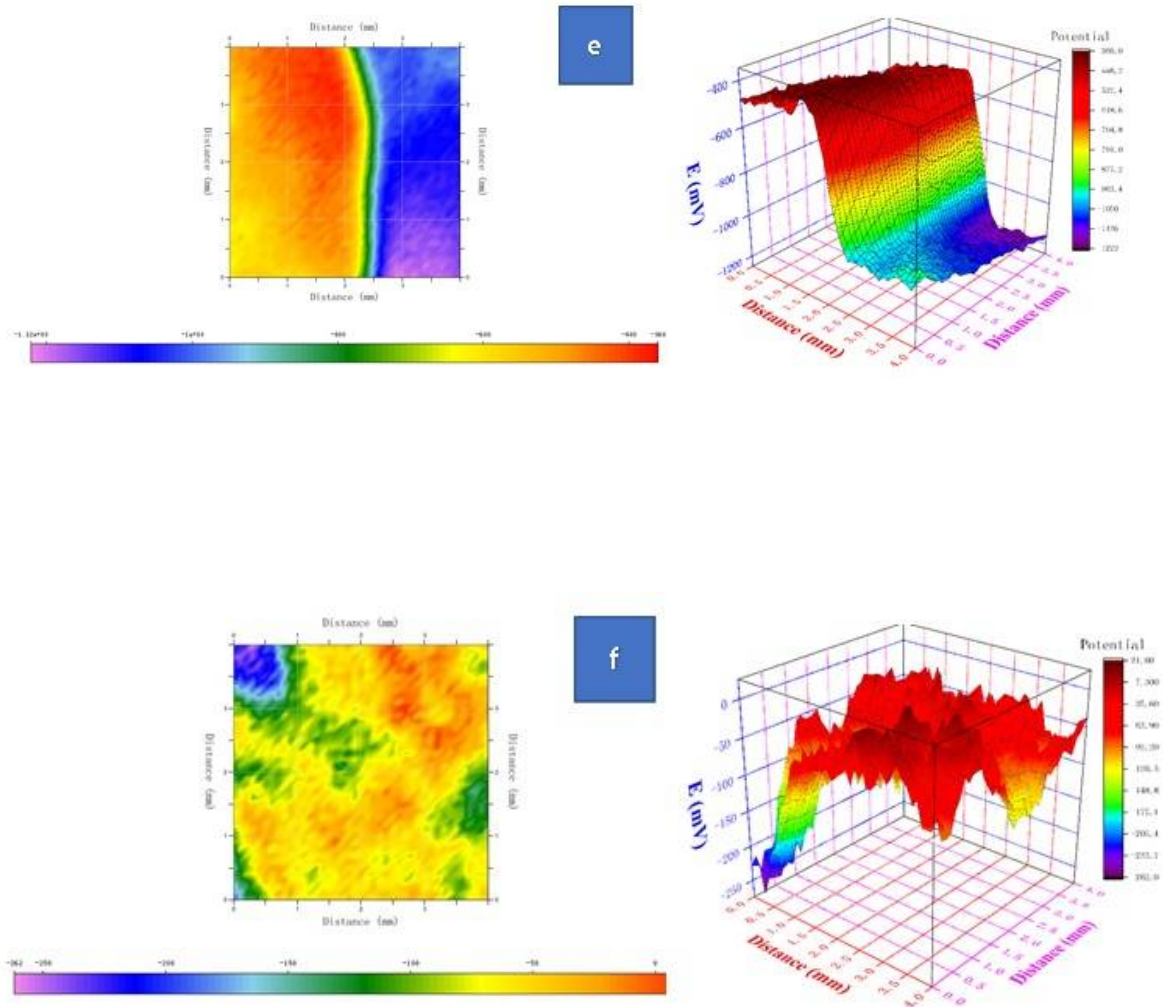


**Figure 12.** SKP spectrum of samples before and after corrosion (a) 2D and 3D figure of pure Al (b) 2d and 3D figure of pure Al after corrosion (c) 2D and 3D figure of pure Cu (d) 2d and 3D figure of pure Cu after corrosion (e) 2D and 3D figure of welded sample at 40 mm/min (f) 2D and 3D figure of welded sample at 40 mm/min after corrosion.